Journal of Materials Chemistry A

Accepted Manuscript

ROYAL SOCIETY OF CHEMISTRY

www.rsc.org/materialsA

Journal Name

RSCPublishing

ARTICLE

A-site deficient perovskite: the parent for *in situ* exsolution of high-active, regenerable nano-particles as SOFCs anode

Cite this: DOI: 10.1039/x0xx00000x

Received 00th January 2012,
Accepted 00th January 2012

DOI: 10.1039/x0xx00000x

www.rsc.org/

Yifei Sun[a], Jianhui Li[b,c,*], Yimin Zeng[d], Babak Shalchi Amirkhiz[d], Mengni Wang[a], Yashar Behnamian[a], Jingli Luo[a,*]

Chemical deposition is widely used to enhance the performance of perovskite anode for solid oxide fuel cells (SOFCs). However, the anodes thus produced still have unsatisfactory activity and experience regenerability problems. For the first time, this paper reports that the *in situ* exsolution of nano Ni could be facilitated on Ni-doped $(La_{0.7}Sr_{0.3})CrO_3$ (LSCNi) anode with A-site deficiency, showing maximum power density of 460 mW cm^{-2} in 5000 ppm H_2S-H_2 compared to only 135 mW cm^{-2} of fuel cell with stoichiometric LSCNi. Besides, the fuel cell also demonstrates desirable redox stability in sour fuel. The introduction of A-site deficiency can help the formation of highly-mobile oxygen vacancies and remarkably enhance the reducibility of Ni nano-particles, thus significantly increase electronic conductivity and catalytic activity simultaneously. Such fabricated perovskite has the potential to be decorated with diverse nano active particles for wide range of applications in industrial fields.

Introduction

Solid oxide fuel cells (SOFCs) have attracted particular attention over the past few decades because of their application potential to lower industrial pollutant emission and increase energy efficiency.(1-4) However, a number of problems, such as unsatisfactory redox stability, still remain to be solved prior to the large scale industrial application of the technology. In SOFCs, Ni-YSZ cermet anode has been widely investigated as it has excellent catalytic activity and superior electrical conductivity.(5) The Ni-YSZ cermets, however, have poor redox stability and weak tolerance against even trace amount of H_2S in fuel gases.(6) Therefore, other alternative anode materials, such as perovskite (ABO_3) with better stability in sour fuel, have been developed for SOFCs.(7, 8) Nonetheless, these materials exhibited much lower intrinsic catalytic activity and conductivity.(9)

To increase the activity of perovskite, active metal catalysts are introduced as catalytic nanoparticles dispersing on the external surface and porous inner surface of perovskite-based anode.(10, 11) These functional materials are usually synthesized using either wet impregnation method(12, 13) or chemical deposition technology(14-16) to generate a structure with catalytic particles attached to the surface of support material through calcination process at high temperatures. However, these methods are time consuming and may lead to the problems of uncontrolled particle sizes and unexpected aggregation of particles.(17) Recently, a more advanced and effective way is developed to introduce nano particles on perovskite oxide, by which the active elements (transitional metal(17, 18) or precious metal(11, 19)) are doped into B-site and then partly *in situ* exsolved out of the lattice as active nanoparticle in reducing atmosphere. The produced nano-catalysts provide more active sites and larger specific surface area to facilitate catalytic reactions. In comparison to the wet impregnation and chemical deposition technologies, this method is time-efficient and can generate nanoparticles with much even dispersion. Besides, the problem of grain coarsening could be also effectively alleviated due to the strong interaction between the nanoparticle and the matrix.

Most of the previous investigations on the application of exsolution in preparing perovskite anode mainly focused on the stoichiometric perovskite oxide with A/B = 1, in which only limited reducible cations were exsolved out, leading to the restricted electrochemical performance. Two recent studies on $La_{0.52}Sr_{0.28}Ni_{0.06}Ti_{0.94}O_3$ perovskite oxides(20) and Fe/Ni-doped $La_{0.2}Sr_{0.25}Ca_{0.45}TiO_3$ (LSCTA) perovskite(21) suggest that more cations can be preferentially exsolved on the surface of the perovskite matrix when the composition of a perovskite oxide is altered to A/B < 1. It is likely that the A-site deficiency could provide an alternative promising way to

"decorate" the perovskite structure with well-dispersed functional nano-particles.

However, to the best of our knowledge, no work has been done so far to assess the electrochemical performance of A-site deficiency perovskite anode in SOFCs. It also remained unclear whether the functional materials of this type would have desirable redox stability in sour fuel. Therefore, the objective of this work is to address the above issues and finds a more promising way to fabricate new functional perovskite materials for industrial SOFCs application. In this paper, Ni-doped LSC (strontium doped lanthanum chromate) perovskite anode with A-site deficiency was prepared using exsolution method and its microstructural properties, electrochemical performances and redox stability in sour fuel were characterized and compared with those of the anode with stoichiometric composition.

Experimental

Fabrication of electrode materials

The glycine nitrate combustion method was used to fabricate the $La_{0.7}Sr_{0.3}CrO_{3-\xi}$, $La_{0.7}Sr_{0.3}Cr_{1-x}Ni_xO_{3-\xi}$ and $La_{0.6}Sr_{0.3}Cr_{1-x}Ni_xO_{3-\xi}$ anode materials for fuel cell test, denoted as LSC, 73LSCNi-x and 63LSCNi-x [where x (mol%) = 0, 5, 10, 15 and 20], respectively. The denotations of each materials are shown in Table I.

Table I Denotation of various materials

Abbreviation	Anode compositions
LSC	$(La_{0.7}Sr_{0.3})CrO_{3-\xi}$,
73LSCNi-15	$(La_{0.7}Sr_{0.3})\ (Cr_{0.85}Ni_{0.15})O_{3-\xi}$
63LSCNi-5	$(La_{0.6}Sr_{0.3})\ (Cr_{0.85}Ni_{0.05})O_{3-\xi}$
63LSCNi-10	$(La_{0.6}Sr_{0.3})\ (Cr_{0.85}Ni_{0.1})O_{3-\xi}$
63LSCNi-15	$(La_{0.6}Sr_{0.3})\ (Cr_{0.85}Ni_{0.15})O_{3-\xi}$
63LSCNi-20	$(La_{0.6}Sr_{0.3})\ (Cr_{0.8}Ni_{0.2})O_{3-\xi}$
63LSCCo-15	$(La_{0.6}Sr_{0.3})\ (Cr_{0.85}Co_{0.15})O_{3-\xi}$
63LSCFe-15	$(La_{0.6}Sr_{0.3})\ (Cr_{0.85}Fe_{0.15})O_{3-\xi}$

Stoichiometric amounts of $La(NO_3)_2{\cdot}6H_2O$, $Sr(NO_3)_2$, $Ni(NO_3)_2{\cdot}6H_2O$, $Cr(NO_3)_3{\cdot}9H_2O$ and glycine were dissolved in deionized water firstly. The molar ratio of glycine to the total content of the metal cations was 2:1. The solution was stirred thoroughly and then heated on a hot plate at 500 ^oC until self-combustion started. The generated powders were ground and further calcined at 1300 ^oC in air for 3 h to produce different anode materials.

Fuel cell fabrication

Fuel cells were fabricated using commercial YSZ disks (FCM, "fuelcellmaterials.com") as electrolyte with the dimension of 100 μm in thickness and 25 mm in diameter. The cathode was the mixture of equal weights of YSZ powder (TOSHO Company), and lanthanum strontium manganite (LSM). The anode was prepared through mixing equal weights of YSZ and prepared anode materials. Both cathode and anode inks were prepared from oxide powders dispersed in terpineol mixed with 10% polyethylene glycol (PEG) as screen printing binder. The electrode inks were deposited onto the YSZ electrolyte disc using screen printing to form a membrane electrode assembly (MEA) with the area of 1 cm^2, and then the cell was sintered at 1100 ^oC for 2 h to form good binding between the electrodes and the electrolyte. The platinum paste and gold paste were painted onto the cathode side and anode side, respectively, to serve as the current collectors.

Single cell tests were performed in a vertical furnace with a coaxial two-tube (inlet and outlet) set-up. The outlet tube was directly sealed (Ceramabond 503, Aremco Products) to the outer edge of the anode side of the single cell electrolyte to avoid leakage of fuel gas and oxygen. A Thermolyne F79300 tubular furnace was used to heat the cell. Hydrogen or hydrogen mixed with 5000 ppm H_2S (5000 ppm H_2S-H_2) (Praxair) as the fuel was fed at a rate of 75 mL min^{-1}. The electrochemical performance of the fuel cell was measured using a Solartron 1287 instrument with 2588 frequencer. The polarization resistance of the cell was estimated based on EIS measured at the open circuit voltage with an AC potential signal of ±10 mV amplitude and the frequency range of 1 MHz to 0.1 Hz.

Redox stability test

A series of redox cycles on the cell was performed at 800 ^oC, with each cycle being conducted through the following steps: (1) the cell was treated with 5000 ppm H_2S-H_2 for 24 h; (2) switching off the anode gas supply and exposing the anode to 5% O_2/N_2 for 2 h; (3) the fuel of 5000 ppm H_2S-H_2 was introduced again until the fuel cell reached a steady state. The power density data were measured after the introduction of the fuel for 30 min.

Materials characterization

The phase structures of synthesized materials were characterized using a Rigaku Rotaflex X-ray diffractometer (XRD) with Cu Kalpha radiation and the obtained data were analyzed using JADE 5.0 software.

The micromorphology of the materials was examined using a JEOL 6301F Scanning Electron Microscopy (SEM). TEM characterizations were conducted using a JEOL JEM2100 transmission electron microscope with Energy-dispersive X-ray spectroscopy (EDX) detector, a JEOL 2100 TEM with electron energy loss spectrometer (EELS) mapping capabilities (operated at 200 kV

accelerating voltage). High angle annular dark field (HAADF) with EDX elemental mapping was used to identify the chemistry of the samples. For TEM analysis, the generated powders were dispersed in alcohol solution. One drop of the prepared suspension was deposited on a carbon-coated TEM Cu grid and dried in air before TEM characterization. The reduced samples for SEM/TEM analysis were prepared in dry 5% H_2/N_2 at the temperature of 800 ^oC for 4 h.

Thermogravimetric analysis (TGA) measurements were conducted using a TA Instruments SDT Q600 under 5% H_2/N_2 from 100 ^oC to 900 ^oC with a flow rate of 20 mL min^{-1} and a heating rate of 20 ^oC min^{-1}.

Hydrogen temperature programmed reduction (H_2-TPR) was performed using an AutoChem II 2920 instrument (Micromeritics, USA) equipped with a thermal conductivity detector (TCD). All samples were treated with Helium at 1000 ^oC for 30 min before TPR. The flow rate of 10% H_2/Ar for analysis was 10 mL min^{-1} and the temperature ramping rate was 10 ^oC min^{-1}.

The values of Gibbs free energy of the reduction reaction of each cation were calculated using HSC 6.0 software.

Van der Pauw four points method was used to measure electrical conductivity of the synthesized samples by ProbStat instruments.

Results

Thermal, structural and morphological analysis

The crystalline structures of the materials with or without Ni doping were examined using XRD technique and are shown in Fig. 1(a). The $La_{0.7}Sr_{0.3}CrO_{3-y}$ (LSC), $La_{0.7}Sr_{0.3}Cr_{0.85}Ni_{0.15}O_{3-\xi}$ (73LSCNi-15) and $La_{0.6}Sr_{0.3}Cr_{0.85}Ni_{0.15}O_{3-\xi}$ (63LSCNi-15) exhibit perovskite structure with orthorhombic unit cells of space group Pnma (62). All of the main peaks are matched well with those of $LaCrO_3$ (JCPDS no.24-1016), indicating that neither B-site doping of Ni in 63LSCNi-15 (or in 73LSCNi-15) nor A-site deficiency in 63LSCNi-15 has any influence on the crystalline structure of perovskite. The reason is that A-site vacancies may act as behave as one kind of dopants with different sizes from those of host cations, similar to accommodation of cations substitution. As shown in Fig. 1(a), 63LSCNi-15 still maintained single-phased perovskite structure after being exposed to 5% H_2/N_2 at 800 ^oC for 4h, and the metallic Ni diffraction peaks were present at 44.5^o and 52^o, indicating the Ni reduction that occurred in perovskite lattice(22). After the re-oxidation in air under calcination condition, the material showed pure perovskite structure again without the formation of the impurity phases such as Ni and/or NiO (Fig. 1(a)), which means that the exsolved metallic Ni was, once again, dissolved into perovskite lattice. This also implies that the A-site deficient material would have good redox structural stability.

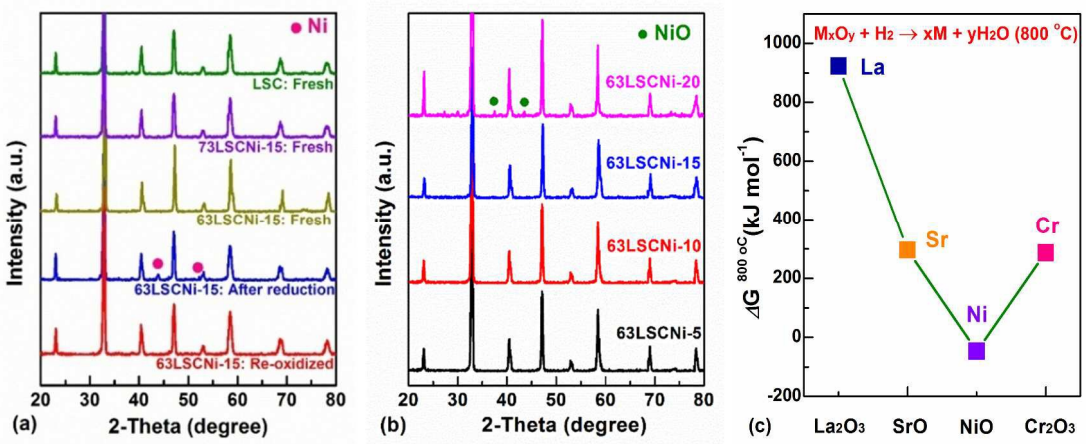

Fig. 1 X-ray diffraction (XRD) patterns and calculated Gibbs free energy of reduction reaction for each element oxide in LSCNi perovskite. (**a**) XRD patterns of the various fresh and treated materials. Among them, 63LSCNi-15 was reduced in 5% H_2/N_2 at 800 ^oC for 4 h and re-oxidized in air at 1300 ^oC for 3h. (**b**) XRD patterns of the fresh 63LSCNi-x with Ni contents, x%, of 5% to 20%. (**c**) The theoretical value of reduction Gibbs free energy for each element oxide in LSCNi-15 perovskite at 800 ^oC. The data are estimated using HSC 6.0 software.

The structural parameters of as-prepared and reduced samples were carried out with Rietveld refinements and the results of cell parameter are shown in Table II below. It was found that the unit cell volume increased with the nickel substitution. It can be explained that when Cr^{3+} is substituted for Ni^{2+}, the oxidation state of the B-site cation should increase from +3 to +4 to maintain charge balance. The smaller radius of higher valence cation will reduce the unit cell size. On the other hand, the data in table also point out that the A-site deficiency results in a decrease of the unit cell volume, in correlation with the literature results on $Sr_{1-1.5x}Pr_xTiO_{3-y}$ (23) and $(Sr_{0.7}La_{0.3})_{1-x}TiO_{3-y}$ perovskites (24). The 63-LSCNi-15 sample was reduced at 800 ^oC in 5%H_2-N_2, and an increase in lattice

parameter with the respect to as-prepared material could be found. The reason should be attributed to the more oxygen vacancy formation resulting in the increase of repulsive force between neighboring cations (25).

Table II Cell parameters of various materials

Samples	a (nm)	b (nm)	c (nm)	V (nm)
LSC	0.5449	0.5463	0.7823	0.2329
73LSCNi-15	0.5428	0.5473	0.7873	0.2339
63LSCNi-15	0.5443	0.5465	0.7820	0.2326
Reduced-63LSCNi-15	0.5448	0.5450	0.7892	0.2343

As shown in Fig. 1(b), the doping of Ni (≤ 15 mol %) had no influence on the formation of pure perovskite structure in A-site deficient materials with orthorhombic symmetry. For 63LSCNi-20, the formation of NiO was detected at the diffraction peaks of 37° and 43° (consistent with the other observation(26)), further confirming that the solubility limit of nickel in LSC perovskite with stoichiometry shall be < 20 mol%. (19) Otherwise, the excessive doping of Ni can result in the formation of NiO after redox cycles. When below the solubility limit, only metallic Ni was detected and the corresponding XRD observations were consistent with the calculated free energy changes of the oxide reductions in LSCNi perovskite as shown in Fig. 1 (c). It is clear that the NiO shall be the only reducible oxide in perovskite because of its negative Gibbs free energy (-46.47 kJ mol^{-1}) at 800 °C, while other metal oxides have positive Gibbs free energies.

Oxygen vacancies play a significant role in the conductivity and catalytic activity of a perovskite material. Thermogravitimetric analysis was applied to measure the amount of oxygen vacancies in different materials from 100 °C to 900 °C with a heating rate of 20 °C min^{-1} in 5% H_2/N_2 and the results are shown in Fig. 2(a). The LSC was the most stable material with the lowest weight loss (0.1%) during the measurement, while the formation of oxygen vacancies in 73LSCNi-15 started at a temperature of ~ 620 °C and the total weight loss was about 0.4%. In contrast with the cases of LSC and 73LSCNi-15, the A-site deficient 63LSCNi-15 started to lose weight at 515 °C and exhibited the highest oxygen vacancies as its weight loss was close to ~ 2.5%. Such remarkable difference indicates that the A-site deficiency could lead to the high conductivity of the material.

Since weight loss accompanies the reduction process, the mass changes during the TGA tests could be used to estimate the quantity of oxygen non-stoichiometry, ξ. Results in Fig. 2(b) indicate that ξ increased from 0.025 to 0.1 after the doping of Ni in B-site of LSC, which was much less than that of the non-stoichiometric A-site composition (ξ = 0.32). Thus, it can be quantitatively inferred that the deficiency in A-site can help the formation of oxygen vacancies in perovskite structure and enhance the mobility of the lattice oxygen. Thus, the catalytic activity of the material can also be facilitated. The high value of ξ for perovskite with A-site deficiency is likely because A-site deficiency can limit the number of intrinsic Schottky defects, which in turn facilitate the diffusion and removal of lattice oxygen in reducing atmosphere.

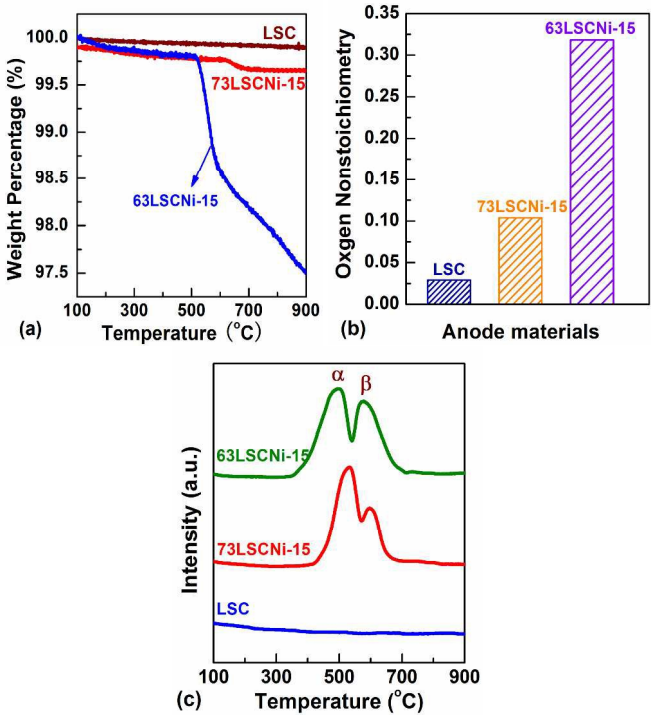

Fig. 2 Thermogravimetric analysis (TGA), quantity of oxygen non-stoichiometry and characterizations of hydrogen temperature-programmed reduction (H_2-TPR) of the various catalysts. (**a**) TGA curves of the fresh LSC, 73LSCNi-15 and 63LSCNi-15 measured in 5% H_2/N_2 with a flow rate of 20 mL min^{-1} from 100 °C to 900 °C at a heating rate of 20 °C min^{-1}. (**b**) The quantity of oxygen non-stoichiometry determined based on the mass change during the TGA test. (**c**) H_2-TPR curves of the fresh LSC, 73LSCNi-15 and 63LSCNi-15. All samples were treated with helium at 1000 °C for 30 min before TPR. The flow rate of 10% H_2/Ar was 10 mL min^{-1} and the temperature ramping rate was 10 °C min^{-1}.

To investigate the reducibility of this series of Ni-doped LSC, the TPR analysis was applied on each sample and the results are shown in Fig. 2(c). There was no obvious peak in the pattern of LSC sample, suggesting that the $La_{0.7}Sr_{0.3}CrO_3$ might not be reduced up to 900 °C, which was consistent with the TGA measurements. The improvement in the reducibility of the Ni-substituted compositions was observed for both 63LSCNi-15 and 73LSCNi-15, indicated by multiple peaks of different Ni states. Previous studies(27, 28) show that the reduction of Ni-substituted LSC perovskite likely occurs through two

main steps: (1) the α-peak at the temperature of~ 500 °C from reduction of Ni^{3+} into Ni^{2+}; and (2) the β-peak at the temperature of ~600 °C, associated with reduction of Ni^{2+} into metallic Ni^0. With the introduction of A-site deficiency in perovskite lattice, the reducibility of Ni was remarkably facilitated. As shown in the Fig. 2 (c), the first reduction peak shifted from 532 °C to 492 °C, and the second reduction peak from 602 °C to 577 °C. Moreover, the ratio of the β-peak area to α-peak area was around 0.67 for 63LSCNi-15, higher than that (0.25) for 73LSCNi-15, a clear indication that A-site deficiency could facilitate the reduction of Ni^{2+} to Ni to generate more Ni nano particles.

SEM and TEM characterizations in Fig. 3 reveal the influence of A-site deficiency on the exsolution of Ni nano particles. After being reduced at 800 °C for 4h, numerous metallic Ni nanoparticles were formed on the A-site deficient 63LSCNi surface [Fig. 3(a)], but only limited Ni particles were produced on the stoichiometric composite [Fig. 3(b)], even though the doping content of Ni in B-site of the samples was same (15%). Such a difference indicates that the A-site deficient perovskite is more prone to exsolution of B-site species than the stoichiometric one.

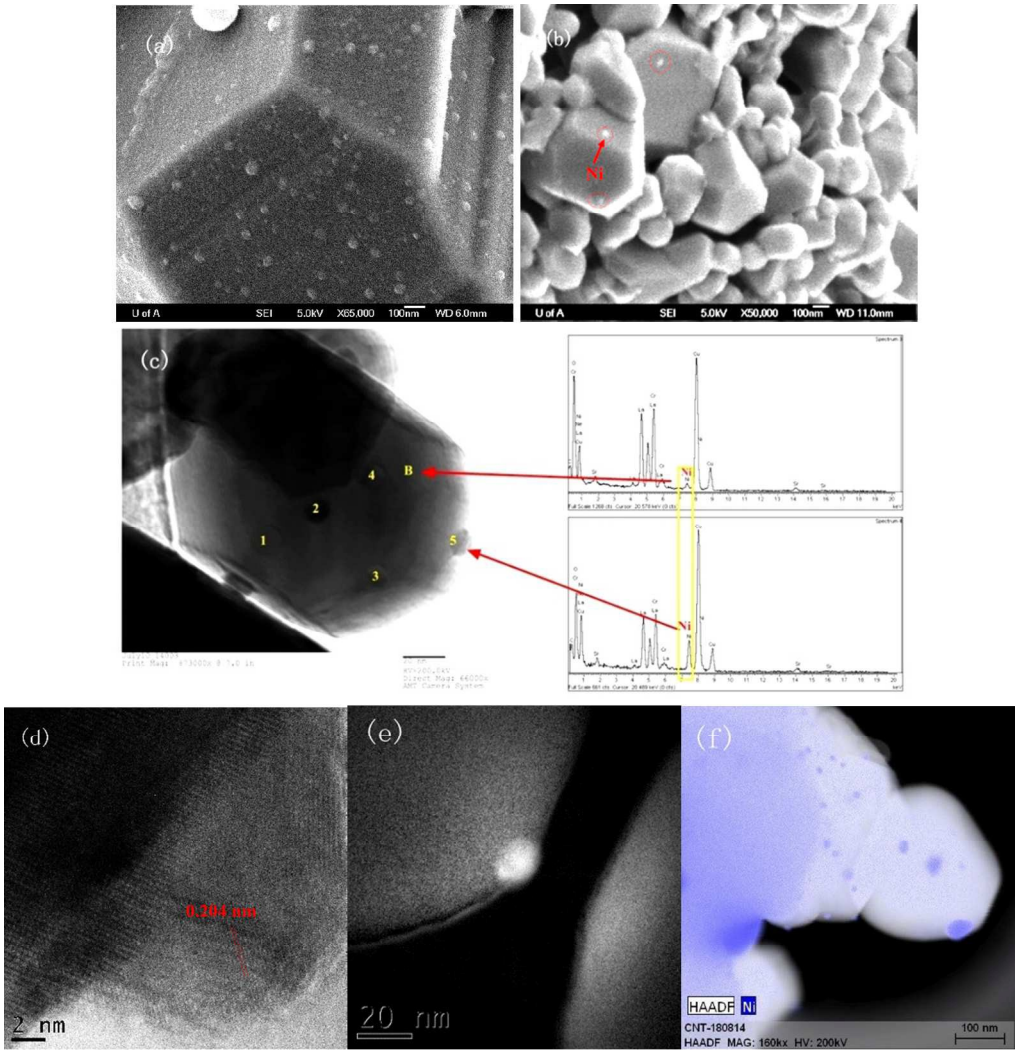

Fig. 3 Scanning electron microscopy (SEM), energy-dispersive X-ray spectroscopy (EDX), transmission electron microscopy (TEM), energy filtered TEM (EFTEM) and high angle annular dark field (HAADF) images for 63LSCNi-15 and 73LSCNi-15 samples. SEM images for (**a**) 63LSCNi-15 and (**b**) 73LSCNi-15 materials reduced at 800 °C for 4 h. (**c**) EDX analysis for point 5 and B of TEM image of 63LSCNi-15 on the left side of (c). (**d**) TEM micrograph of the exsolved nano-particle anchored on bulk material. (**e**) EFTEM image of a Ni particle. (f) HAADF image of a 63LSCNi-15 particle overlaid with EDX elemental map of Ni-highlighting nanoparticles.

The chemical compositions of the nano particles anchored on the surface of bulk material and the bulk material were examined using EDX analysis and the results are shown in Fig. 3(c). It is clear that the chemical composition of the bulk (point B) was quite different

from the nano particle (point 5) where the much stronger Ni peak was found.

Detailed structural characterization of the nano particle using TEM technique is depicted in Fig. 3(d). Clear lattice image was observed only for the particles whose arrangement of atom planes was parallel with the direction of the electron beam. The spacing between two adjacent lattice fringes was 0.206 nm, close to the (111) planes of fcc Ni (JCPDS 01-1258, d(111) = 0.2030 nm). Fig. 3(e) shows the Ni mapping obtained from the energy loss windows centered at the C K-ionization edge at 855 eV, and confirms that the exsolution of nano particle was composed of metallic Ni. Fig. 3(f) shows the HAADF image of a 63LSCNi-15 particle overlaid with EDX elemental map of Ni-highlighting nanoparticles. The presence of well-dispersed bright spots with high density corresponds to the exsolved Ni nanoparticles on the perovskite scaffold, which is consistent with the observations described above.

Electrochemical Performance

To assess the electrochemical performance of 63LSCNi-15 and 73LSCNi-15 anodes, the I-V and power density curves of the fuel cells with 63LSCNi-15 and 73LSCNi-15 anodes were measured using H_2 and 5000 ppm H_2S-H_2 as the fuels at 800 °C and the results are shown in Fig. 4 (a) and (b), respectively.

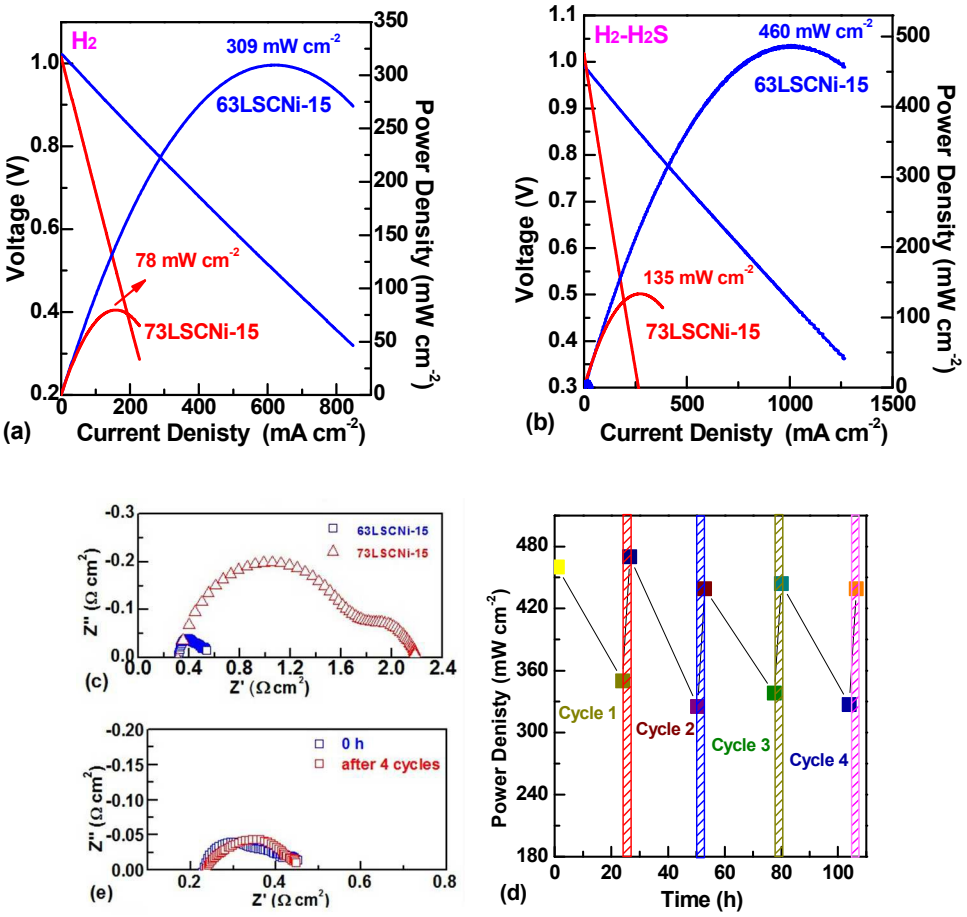

Fig. 4 Fuel cell performances with the various anodes in H_2 or 5000 ppm H_2S-H_2. Current density–voltage and power density curves for fuel cells with 63LSCNi-15 and 73LSCNi-15 anodes using (a) pure H_2 fuel and (**b**) 5000 ppm H_2S-H_2 fuel at 800 °C. (**c**) EIS for the cells with 63LSCNi-15 and 73LSCNi-15 anodes fueled with 5000 ppm H_2S-H_2 at 800 °C. (**d**) The redox test results for 63LSCNi-15-YSZ/YSZ/YSZ-LSM fuel cell at 800 °C during four 26 h-cycles. In each cycle, the cell was treated with 5000 ppm H_2S-H_2 for 24 h and then recovered via the *in situ* treatment of 5% O_2/N_2 for 2 h (hatched period). Then the fuel was introduced again and the power density was measured after the introduction of fuel for 30 min. (**e**) The comparison of EIS results for the cell using 63LSCNi-15 anode before and after 4 redox cycle test in (d).

In H_2 fuel, the maximum power density of the cell with 63LSCNi anode was 309 mW cm^{-2}, which was about four times higher than that obtained from 73LSCNi anode. In comparison of Fig. 4 (a) and (b), it is clear that the addition of H_2S enhanced the anode activity and

provided better cell performance. The maximum power density of the 63LSCNi-15 cell tested in 5000 ppm H_2S-H_2 at 800 °C was about 460 mW cm^{-2} with the maximum current density higher than 1200 mA cm^{-2}. The SOFCs with 73LSCNi-15 anode only generated the power density output of 135 mW cm^{-2} with the maximum current density < 300 mA cm^{-2}. The promoting effect of H_2S for the oxidation of H_2 on perovskite-based anode for SOFCs has been demonstrated and discussed elsewhere (29-31). One possible mechanism is that at room temperature the S absorbed on oxygen can form H_2-S-O bond which may serve as an effective carrier for H_2 to react with oxygen ions. The H_2S itself could be considered as H_2 carrier. Since the decomposition of H-S bond in H_2S (363 kJ mol^{-1}) is easier than that via breaking H-H bond (436 kJ mol^{-1}) directly, the lower energy barrier for decomposition of fuel facilitate the reaction and enhance the electrochemical performance.

Fig. 4(c) shows the corresponding electrochemical impedance spectra (EIS) of 73LSCNi-15 and 63LSCNi-15 fuel cells fueled with 5000 ppm H_2S-H_2 at 800 °C. All the EIS data were obtained only after the cell had reached its steady state. Obviously, both anode catalysts were active for the conversion of H_2, and the introduction of A-site deficiency significantly improved the cell performance. The electrolyte resistance of each cell was ~ 0.3 Ω cm^2. The activation polarization resistance of the 63LSCNi-15 anode measured in 5000 ppm H_2S-H_2 at 800 °C was about 0.26 Ω cm^2 that was only 1/6 of that of 73LSCNi-15, meaning that the A-site deficiency could remarkably improve the electrochemical performance of anode because of the larger amount of Ni particles with high catalytic activity.

It is well recognized that one of the biggest challenges for Ni-based cermet anode is its poor redox stability. Although the anode material is kept in reducing atmosphere during operating process, the re-oxidation of Ni to NiO could occur because of imperfect sealing of anode chamber or unexpected shutdown of the operating system. As the accumulated NiO oxides occupy more volume than Ni particle(32), such dimensional change after redox cycles would result in the formation and propagation of the micro-cracks across the anode and electrolyte, leading to degraded performance or full failure of the SOFC cell. Based on the XRD characterization (Fig. 1), we can see that A-site deficient materials exhibited high structural redox stability upon exposure to oxidizing and reducing atmosphere.

To test the redox stability of the 63LSCNi-15 anode in H_2S containing fuel, the cell was periodically treated with 5000 ppm H_2S-H_2 at 800 °C for 24 h, followed by a recovery process of *in situ* treatment in 5% O_2/N_2 for 2 h. The reason behind using oxygen treatment is that it can be more effective than H_2O in terms of removing the sulfur atoms adsorbed onto the Ni surface.(33) Subsequently, the fuel of 5000 ppm H_2S-H_2 was introduced for 30 min to reach the stable state before the next cycle test. Fig. 4 (e) shows the maximum power density of the cell with 63LSCNi-15 anode in four redox cycles with total test duration of more than 100 h. In the first cycle, the cell had initial power density of 460 mW

Discussion cm^{-2} and final density of 340 mW cm^{-2} after 24 h treatment in 5000 ppm H_2S-H_2. The degradation may be due to the sintering of exsolved metal nanoparticles and the coverage of active sites by sulfur. After the cell was treated in an oxidative atmosphere for 2 h, the cell performance was restored to the initial power density level (~ 460 mW cm^{-2}), as shown in the Fig. 4(e), suggesting that the exsolved nanoparticle could re-dissolve into the lattice to return to its oxidized state and the absorbed sulfur be oxidized and removed. When the fuel was introduced again, the nano Ni particle re-exsolved out of the lattice again and the performance can be completely regenerated. During the 4 redox cycles, the cell could be fully recovered by *in situ* treatment without noticeable degradation in power generation.

Fig. 4(e) is the EIS spectra of 63LSCNi-15 anode before and after 4 redox cycles at 800 °C. No obvious increase in the polarization resistance or the ohmic resistance was found. The results confirmed that the catalyst could be fully regenerated and the microstructure of 63LSCNi-15 is strongly tolerant to redox cycle. Otherwise, the cracks would occur across the cell, resulting in an increase in ohmic resistance.

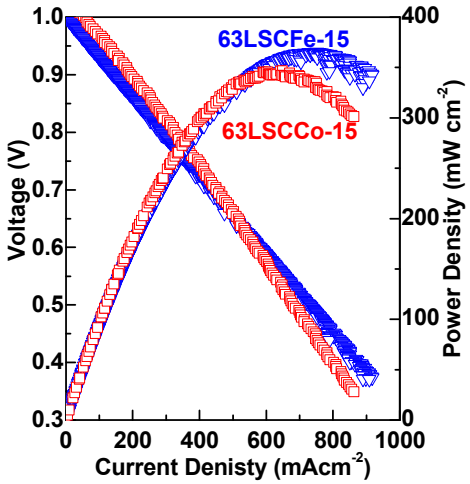

Fig. 5 Current density–voltage and power density curves for fuel cells with Fe doped LSC and Co-doped LSC anodes in 5000 ppm H_2S-H_2 at 800 °C.

To evaluate the generality of this strategy, Co and Fe doped LSC perovskite anodes were also prepared using the same experimental procedure stated in this paper and their electrochemical performances were assessed in 5000 ppm H_2S-H_2. The maximum power densities of the fuel cells with anodes of 63LSCFe-15 and 63LSCCo-15 were 365 mW cm^{-2}, and 345 mW cm^{-2}, respectively (shown in Fig. 5). This results clearly reiterate that the Co and Fe doped LSC with A-site deficiency also obtain desirable catalytic activity toward the oxidation of fuel and could be regarded as potential anodes for SOFCs.

Therefore, we believe that this approach is a promising way to synthesize a variety of functional perovskite materials with high electrochemical performance, attractive redox stability and enhanced sulfur resistance for energy production.

An excellent anode material for SOFCs should meet the requirements of high catalytic activity for oxidation of fuel, high ionic and electronic conductivities, and good redox stability. In our investigation, the enhancement of electrochemical performance of 63LSCNi-15 anode could be firstly attributed to the exsolution of the widely dispersed nano Ni particles. The introduction of A-site deficiency alters the stoichiometric composition to help the exsolution of Ni in B-site. For A-site deficient anode, the main driving force of Ni exsolution is the decrease in Gibbs free energy [Fig. 1(c)] through the reduction of Ni from oxidized state in the chromite lattice. Then, Ni precipitates onto its surface under reducing atmosphere since Ni^{2+} is thermodynamically unstable in $LaCrO_3$ lattice at 800 °C and $P_{O2}<10^{-14}$ atm.(19)

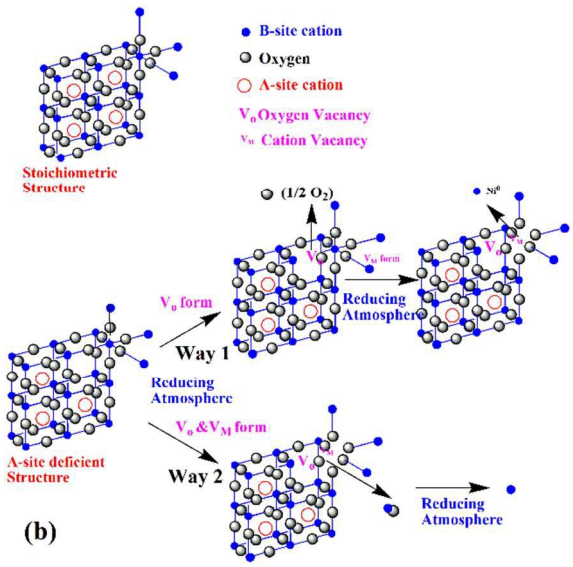

Fig. 6 The schematic of generation of oxygen vacancies and Ni exsolution process for perovskite with A-site deficiency. The simulated figure was drawn using ChemDraw 8.0.

In addition to the facilitation of the exsolution of catalytically active nano-Ni, the promoted diffusion of oxygen in lattice could be regarded as another important reason for the enhancement of performance. Fig. 6 is the schematic of generation of oxygen vacancies and exsolution process for perovskite with A-site deficiency. During the treatment in reducing atmosphere, the oxygen vacancies would be introduced, which destabilized the perovskite lattice and resulted in the spontaneous exsolution of B-site species. Other possible process is that the oxygen vacancies and B-site cation vacancies could also be simultaneously introduced by treatment in reducing atmosphere and then the metal oxide could be converted to corresponding metal exsolved from the lattice. As shown in Fig. 2 (b), the amount of oxygen vacancies in A-site deficient perovskite was much higher than that in the perovskite with stoichiometric composition, leading to better ionic conductivity as well as larger amount of exsolved Ni. It is worth mentioning that the exsolution of metallic Ni would also increase electronic conductivity of the material, which in turn makes contribution to the better performance of the material. The electrical conductivity of various materials are tested and the results are reported in Fig. 7 below as a function of temperature. For the purpose of comparison, data for LSC without any substitution are also included in Fig. 7 as well. In each test, the measurement was conducted for 30 minutes to reach equilibrium. Also as expected, pure LSC showed the lowest conductivity. And the 63LSCNi-15 exhibited the highest conductivities that is higher than the 73LSCNi-15 material, indicating that the introduction of A-site deficiency could enhance the conductivity of the material.

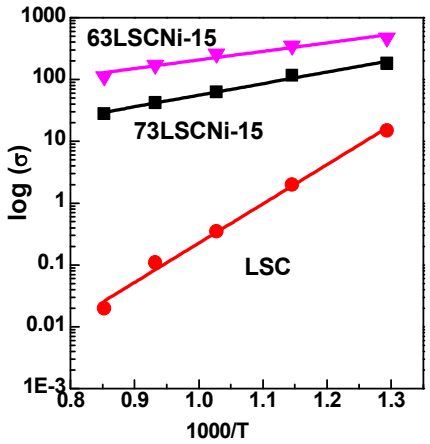

Fig 7. Electrical conductivity test of different material in air as a function of temperature.

The conductivity of A-site deficient materials in reducing atmosphere will be confirmed in our future work.

Last but not least, previous research has shown the introduction of A-site deficiency promote the ion diffusion which facilitate the sinterbility of the materials and yields larger grains providing more available hopping sites for cations.(35) Thus, another reason for the excellent performance of the A-site deficiency perovskite is that the diffusion of nickel ions could be facilitated, resulting in more metallic nickel particles were exsolved out.

Compared to the traditional Ni-based anode materials, the A-site deficient perovskite not only exhibits comparable electrochemical performance but also shows desirable redox stability in sour fuel, achieving both in sour fuel was once considered as one of great challenges for Ni/YSZ anode. The XRD results have demonstrated that after exposure to oxidizing atmosphere, the reduced materials were turned into perovskite again without the formation of impurities, indicating that the exsolved metallic Ni had dissolved into the perovskite lattice. The

phenomenon of the movement of Ni into and out of the lattice upon redox cycling was also found by other researchers.(16, 36-37) The unique characteristic of redox stability of the material in both sweet and sour gases reported in this work suggests that it may be applicable to utilize redox cycling to fully recover performance loss for fuel cells after prolonged reaction.

Conclusions

Ni-doped LSC perovskite oxide anodes with A-site deficiency were successfully prepared. The A-site deficiency plays a key role in driving the exsolution of Ni in B-site, resulting in a significant enhancement in the diffusion of lattice oxygen and the exsolution of Ni^{2+} to metallic Ni^0. The A-site deficient LSCNi materials exhibit promising electrochemical performance and attractive redox stability in 5000 ppm H_2S-H_2. Furthermore, the generality of this anode preparation method can be applied for the exsolution of other active transition metals. Therefore, this approach presents a promising way to greatly improve the catalytic properties and stability of electrode materials. The significance of the material characteristics presented in this paper lies in the much broader application potential of the methodology for fabricating next generation electrode materials in the fields of energy conversion and energy storage in general.

Acknowledgements

This work is supported by Natural Sciences and Engineering Research Council (NSERC) of Canada Strategic Project Grant and the National Natural Science Foundation of China under grant 21303141. The authors gratefully acknowledge Jing Shen at University of Alberta for her assistance in measuring H_2-TPR curves.

Notes and references

[a] Department of Chemical and Materials Engineering，University of Alberta，Alberta, Canada, T6G 2V4. *E-mail: Jingli.Luo@ualberta.ca.*
[b] National Engineering Laboratory for Green Chemical Productions of Alcohols-Ethers-Esters, College of Chemistry and Chemical Engineering, Xiamen University, Xiamen, China, 361005. *E-mail: jhli@xmu.edu.cn.*
[c] Department of Chemistry and Applied Chemistry, University of Changji, Changji, China, 831100.
[d] Canmet MATERIALS, Natural Resources Canada, Hamilton, Ontario, Canada, L8P 0A5.

References

1 D. E. Fowler, J. Haag, C. Boland, D. M. Bierschenk, S. A. Barnett and K. R. Poeppelmeier, *Chem. Mater.*, 2014, **26**, 3113-3120.
2 M. Chen, S. Paulson, V. Thangadurai and V. Birss, *J. Power Sources*, 2013, **236**, 68-79.
3 E. D. Wachsman and K. T. Lee, *Science*, 2011, **334**, 935-939.
4 P. I. Cowin, C. T. G. Petit, R. Lan, J. T. S. Irvine and S. Tao, *Adv. Energy Mater.*, 2011, **1**, 314-332.
5 W. Wang, C. Su, Y. Wu, R. Ran and Z. Shao, *Chem. Rev.*, 2013, **113**, 8104-8151.
6 E. Brightman, D. G. Ivey, D. J. L. Brett and N. P. Brandon, *J. Power Sources*, 2011, **196**, 7182-7187.
7 S. Boulfrad, M. Cassidy, E. Djurado, J. T. S. Irvine and G. Jabbour, *Int.. J. Hydrogen Energy*, 2013, **38**, 9519-9524.
8 L. M. Petkovic, V. Utgikar and S. N. Rashkeev, *J. Phys. Chem. C*, 2011, **115**, 8709-8715.
9 X. Zhou, N. Yan, K. T. Chuang and J. Luo, *RSC Adv.*, 2014, **4**, 118-131.
10 H. Tanaka, M. Taniguchi, M. Uenishi, N. Kajita, I. Tan, Y. Nishihata, J. Mizuki, K. Narita, M. Kimura and K. Kaneko, *Angew. Chem.*, 2006, **45**, 5998-6002.
11 Y. Nishihata, J. Mizuki, T. Akao, H. Tanaka, M. Uenishi, M. Kimura, T. Okamoto and N. Hamada, *Nature*, 2002, **418**, 164-167.
12 S. P. Jiang, *Int.. J. Hydrogen Energy*, 2012, **37**, 449-470.
13 S. Lee, G. Kim, J. M. Vohs and R. J. Gorte, *J. Electrochem. Soc.*, 2008, **155**, B1179.
14 J. Lu, B. Fu, M. C. Kung, G. Xiao, J. W. Elam, H. H. Kung and P. C. Stair, *Science*, 2012, **335**, 1205-1208.
15 A. Lintanf, *Solid State Ionics*, 2008, **178**, 1998-2008.
16 L. Adijanto, V. Balaji Padmanabhan, R. Kungas, R. J. Gorte and J. M. Vohs, *J. Mater. Chem.*, 2012, **22**, 11396-11402.
17 C. Arrivé, T. Delahaye, O. Joubert and G. Gauthier, *J. Power Sources*, 2013, **223**, 341-348.
18 V. B. Vert, F. V. Melo, L. Navarrete and J. M. Serra, *Appl. Catal. B: Environ.*, 2012, **115-116**, 346-356.
19 W. Kobsiriphat, B. D. Madsen, Y. Wang, M. Shah, L. D. Marks and S. A. Barnett, *J. Electrochem. Soc.*, 2010, **157**, B279.
20 D. Neagu, G. Tsekouras, D. N. Miller, H. Menard and J. T. Irvine, *Nat. chem.*, 2013, **5**, 916-923.
21 A. Yaqub, N. K. Janjua, C. Savaniu and J. T. S. Irvine, *Int. J. Hydrogen Energy*, 2015, **40**, 760-766.
22 Y. Wang, L. Wang, N. Gan, Z.-Y. Lim, C. Wu, J. Peng and W. G. Wang, *Int. J. Hydrogen Energy*, 2014, **39**, 10971-10979.
23 A.V. Kovalevsky, A.A. Yaremchenko, S. Populoh, A. Weidenkaff and J.R. Frade, *J. Phys. Chem. C*, 2014, **118**, 4596-4606.
24 M. Mori, K. Nakamura and T. Itoh, *J. Fuel Cell Sci. & Tech.*, 2012, **9**, 021007.
25 E. Lay, M. Benamira, C. Pirovano, G. Gauthier and L. Dessemond, *Fuel Cells*. 2012, **12**, 265-274.
26 W. Li, J. N. Reimers and J. R. Dahn, *Solid State Ionics*, 1993, **67**, 123-130.
27 A. Jahangiri, H. Aghabozorg and H. Pahlavanzadeh, *Int.. J. Hydrogen Energy*, 2013, **38**, 10407-10416.
28 K. Rida, M. A. Peña, E. Sastre and A. Martinez-Arias, *J. Rare Earths*, 2012, **30**, 210-216.
29 S.H. Cui, J.H. Li, X.W. Zhou, G.Y. Wang, J.L. Luo, K. T. Chuang, Y. Bai and L.J. Qiao, *J. Mater. Chem. A*, 2013, **1**, 9689-9696.
30 M. Roushanafshar, J.-L. Luo, A. L. Vincent, K. T. Chuang and A. R. Sanger, *Int. J. Hydrogen Energy*, 2012, **37**, 7762-7770.
31 J.H. Li, X.Z. Fu, J.L. Luo, K. T. Chuang and A. R. Sanger, *J. Power Sources*, 2012, **213**, 69-77.
32 M. Ettler, H. Timmermann, J. Malzbender, A. Weber and N. H. Menzler, *J. Power Sources*, 2010, **195**, 5452-5467.
33 J.H. Wang and M. Liu, *J. Power Sources*, 2008, **176**, 23-30.
34 A. L. Sauvet and J. T. S. Irvine, *Solid State Ionics*, 2004, **167**, 1-8.
35 D. Neagu and J. T. S. Irvine, *Chem. Mater.*, 2011, **23**, 1607-1617.
36 H. Tanaka, M. Taniguchi, M. Uenishi, N. Kajita, I. Tan, Y. Nishihata, J. i. Mizuki, K. Narita, M. Kimura and K. Kaneko,

Angew. Chem. Int. Ed., 2006, **45**, 5998-6002.
37 D. M. Bierschenk, E. Potter-Nelson, C. Hoel, Y. Liao, L. Marks, K. R. Poeppelmeier and S. A. Barnett, *J. Power Sources*, 2011, **196**, 3089-3094.

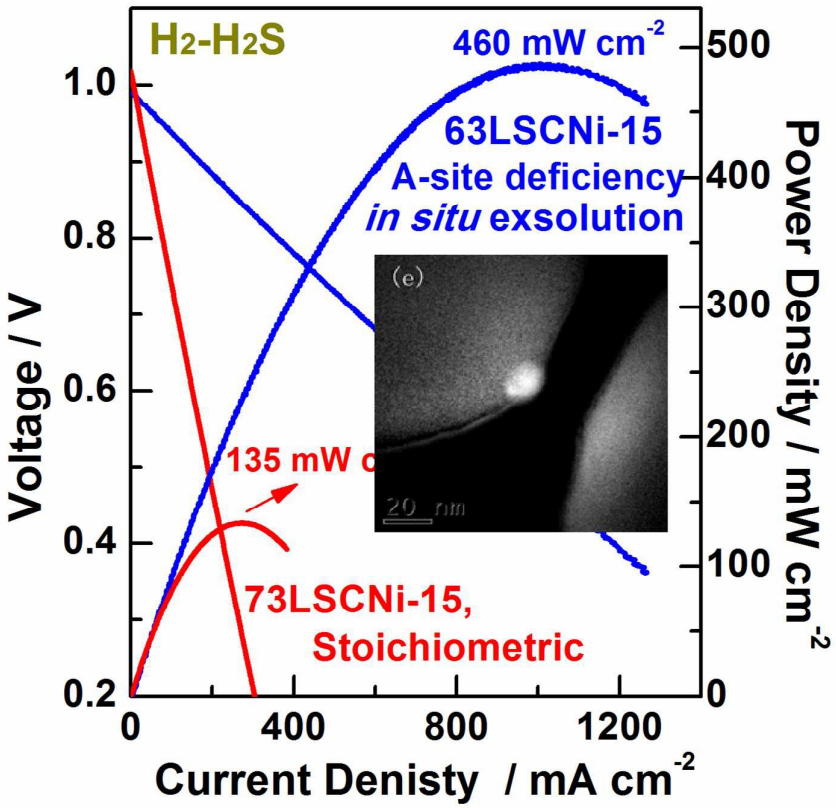

The *in situ* exsolution of nano Ni could be facilitated on Ni-doped $LaSrCrO_3$ anode with A-site deficiency. The introduction of A-site deficiency can help the formation of highly-mobile oxygen vacancies and remarkably enhance the reducibility of Ni nanoparticles, leading to the in-situ exsolution of nano Ni particles and a significant increase in electronic conductivity and catalytic activity simultaneously.